Nano Research

Open Access

Research Article

Unlocking high catalytic activity of mesoporous phytic acid-doped poly(m-phenylenediamine) for electrochemical reduction of biomass-derived cinnamaldehyde to 3-phenylpropanol

Haoran Wu[1], Runlu Yang[1], Chang Su[1], Haishan Xu[2], Tianyu Xiao[2], Chen Li[2], Weixia Zhu[1] ✉, and Yiyong Mai[2] ✉

[1] *School of Chemical Engineering, Zhengzhou University, Zhengzhou 450001, China*
[2] *State Key Laboratory of Synergistic Chem-Bio Synthesis, School of Chemistry and Chemical Engineering, Frontiers Science Center for Transformative Molecules, Shanghai Key Laboratory of Electrical Insulation and Thermal Ageing, Shanghai Jiao Tong University, Shanghai 200240, China*

Cite this article: *Nano Research*, **2026**, *19*, 94908452. https://doi.org/10.26599/NR.2026.94908452

ABSTRACT: The design of metal-free electrocatalysts for efficient biomass-based cinnamaldehyde (CAL) conversion to high-value-added 3-phenylpropanol (HCOL) and the insight into their catalytic mechanism have drawn considerable attention. However, they remained challenging due to the unclear complicated hydrogenation pathways. Here, metal-free mesoporous polymer-based electrocatalysts were synthesized, for the first time, for the electrochemical hydrogenation of CAL to HCOL. The catalysts consist of phytic acid (PA)-doped mesoporous poly(m-phenylenediamine) (coined meso-PA/PmPD) with high specific surface areas up to 95.3 m^2/g. The optimized meso-PA/PmPD exhibits a record-high performance with high Faradaic efficiency (93.5%) and selectivity (97.5%), far surpassing all the reported electrocatalysts (Faradaic efficiency < 55% and selectivity < 25%). Mechanistic studies reveal that meso-PA/PmPD induces the parallel-configuration adsorption of CAL via π–π and hydrogen-bonding interactions, reducing the energy barriers for CAL carbonyl hydrogenation with active hydrogen (H^*) to COL and its subsequent hydrogenation to HCOL, thereby boosting the HCOL selectivity. Meanwhile, an appropriate PA doping amount accelerates water dissociation to generate H^* and interfacial charge transfer. The mesoporous structure facilitates CAL mass transport into the catalyst interior to promote its conversion. This study provides novel insight into the electroreduction mechanism of CAL, guiding the design of high-performance biomass-conversion electrocatalysts through rationally structural engineering of porous polymers.

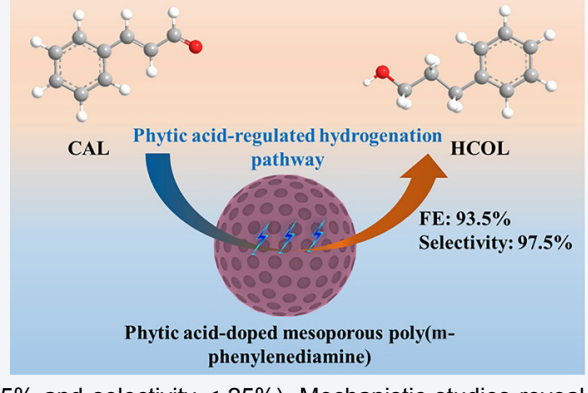

KEYWORDS: porous polymer, electrocatalysis, biomass conversion, cinnamaldehyde, 3-phenylpropanol

1 Introduction

With the excessive consumption of fossil energy and the continuous deterioration of ecological environment, the conversion of renewable biomass into high-value-added chemicals has attracted great attention [1–3]. In this context, the hydrogenation of cinnamaldehyde (CAL) derived from natural cinnamon to produce valuable chemicals has been considered as a sustainable route. Among the different products of cinnamaldehyde, 3-phenylpropanol (HCOL) is an important precursor and/or critical intermediate in the pharmaceutical industries with medicinal properties that can reduce cholesterol and promote bile secretion [4]. In addition, it is also widely used in food, beverage, and cosmetic industries [5]. Currently, the production of HCOL mainly comes from the plant extraction and industrial thermo-catalytic synthesis. However, these processes still face a host of challenges, such as harsh reaction conditions (e.g., high temperature (80–150 °C), high pressure (1–3 MPa), and strong acid) and high-cost noble metal-based catalysts (e.g., Pt-, Pd-, and Ru-based catalysts) [6, 7]. Therefore, it is desirable to develop mild strategies to convert CAL into HCOL.

Electrocatalytic hydrogenation has emerged as an appealing

Received: December 9, 2025; **Revised:** January 14, 2026
Accepted: January 15, 2026

✉Address correspondence to Weixia Zhu, zhuweixia@zzu.edu.cn; Yiyong Mai, mai@sjtu.edu.cn

strategy owing to its mild reaction conditions, specifically, utilizing water as the hydrogen donor under ambient temperature and pressure [8–12]. By obviating the need for high-pressure H_2 and often-toxic homogeneous catalysts, this approach offers a safer and more sustainable alternative to conventional thermal hydrogenation processes. It has been extensively employed for the valorization of organic compounds, biomass, N_2, CO_2, and wastewater streams. These advantages make it particularly promising for green synthesis in fine chemical and pharmaceutical manufacturing [13]. In particular, the electrocatalytic hydrogenation of renewable CAL to produce HCOL has been considered as one of the most important reactions in the field of biomass conversion. Currently, most of the reported electrocatalysts for CAL hydrogenation are metal-based materials, including Pd/SnO_2, CoS_{2-x}, Pt/MoO_3, and Ru/Ta_2O_5 [14–18]. Although great efforts have been made, the best performance reported to date has only achieved a moderate Faradaic efficiency (FE) of less than 55.0%, with a low selectivity of 24.6% (Table S1 in the Electronic Supplementary Material (ESM)). In addition, the intrinsic reaction mechanisms of the electrochemical hydrogenation of CAL to HCOL have still remained unclear. Therefore, it is desirable to design low-cost non-metallic electrocatalysts and gain deeper understanding of the reaction mechanisms for the electrocatalytic hydrogenation of CAL to HCOL.

From the molecular structure of CAL, it is known that CAL features an aromatic ring linked to an aldehyde group via a α,β-unsaturated C=C bond (Fig. S1 in the ESM). The electrocatalytic hydrogenation of CAL to produce HCOL involves the hydrogenation of both the α,β-unsaturated C=C bond and the aldehyde group. To achieve their hydrogenations, the parallel-configuration adsorption of CAL on the surfaces of catalysts is considered as a crucial step (Fig. S1 in the ESM) [14, 18]. This parallel-configuration formation primarily relies on the interactions between the catalyst and the aromatic ring/aldehyde of CAL. However, the conventional metal-based catalysts generally fail to achieve such parallel-configuration adsorption due to their weak Lewis acidic and/or insufficient d–π electronic interactions. Recently, mesoporous polymer-based electrocatalysts have aroused widely interest due to their high surface areas, diverse organic linkers, adjustable functionality, and high stability [19]. Various polymer-based materials (e.g., poly(3,4-ethylenedioxythiophene): polystyrenesulfonate (PEDOT:PSS), polypyrrole, polydopamine, poly(5,5'-divinyl-2,2'-bipyridine), and polytriazine) have been engineered for the electrocatalytic biomass conversion, including the electrochemical conversion of ethanol, 5-hydroxymethylfurfural, benzyl alcohol, furfural, furfuryl alcohol, and glucose [20–23]. These polymeric catalysts exhibit distinct structural and electronic advantages over traditional inorganic counterparts, such as tunable functional groups, flexible molecular skeletons, and adjustable conductive properties, which enable efficient modulation of the adsorption energy of biomass-derived intermediates on the catalyst surface. In addition, their abundant functional groups such as aromatic ring, –OH, C=O, and –NH_2 can enhance the adsorption of aromatic and/or oxygen-containing groups (e.g., –CHO and –OH) through the π–π, hydrogen-bonding, and electrostatic interactions [19]. In particular, rational functionalization of mesoporous polymers structure can endow them with a capability to activate specific functional groups and/or rapid charge transport [24]. For example, Ma et al. reported that the introduction of aromatic naphthalene structures into porous polycarbazole can enhance the adsorption selectivity toward aromatic compounds (benzene and 3-methylthiophene) via π–π interaction between the naphthalene rings of porous polycarbazole and the planar π-electron clouds of the aromatic compounds [25]. Recently, Liu et al. demonstrated that incorporating thiophene moieties into polymeric carbon nitride framework can effectively extend the π-conjugated network, thereby significantly enhancing the charge transport capability of polymers [26]. Phytic acid (PA) is a natural compound derived from seeds and grains [27]. Owing to its multiple phosphate protons, PA can protonate amine and/or imine groups of polymers when incorporating PA into polymers, thus enhancing the conductivity of polymers containing these functional groups [28–30]. In addition, PA can provide rich hydrogen-bonding sites, thus improving polymer's adsorption capacity. Inspired by the advantages of polymer catalysts and PA, the construction of PA-doped mesoporous conductive polymers to simultaneously enhance the parallel adsorption of CAL and charge transport holds promise to enhance the FE and selectivity of electrochemical hydrogenation of CAL to HCOL. However, to our knowledge, there have been no reports on this concept thus far.

Here, a series of PA-doped spherical mesoporous poly(m-phenylenediamine) (meso-PA/PmPD) composite nanospheres were prepared through a block copolymer templated self-assembly strategy (Fig. 1). The average diameter of the meso-PA/PmPD spheres locates in the range of 126–246 nm with a pore size of approximately 7.5 nm. When employed as electrocatalysts for the electrochemical hydrogenation of CAL to HCOL, the optimized meso-PA/PmPD catalyst exhibits a record-high electrocatalytic performance with high FE (93.5%) and selectivity (97.5%) of HCOL, outperforming those of all the reported electrocatalysts significantly (Table S1 in the ESM). Mechanism studies demonstrated that the meso-PA/PmPD can induce the parallel-configuration adsorption of CAL through the π–π and hydrogen-bonding interactions, which reduced the energy barriers for the hydrogenation of CAL carbonyl group with active hydrogen (H*) species to the cinnamyl alcohol (COL) and the subsequent hydrogenation of COL to HCOL, thereby largely boosting the selectivity of HCOL. In addition, an appropriate amount of doped PA may accelerate water dissociation to generate H* species and the interfacial charge transfer rate. The mesoporous structure promotes the mass transport of CAL into the internal space of the catalyst, thus promoting the conversion of CAL. These synergistic effects induce the excellent electrocatalytic performance.

2 Experimental

2.1 Materials

1-Butyl-3-methylimidazolium tetrafluoroborate (BmimBF$_4$, 98%) was purchased from Lanzhou Institute of Chemical Physics, Chinese Academy of Sciences. PA (50 wt.%), m-phenylenediamine (mPD, 99%), and ammonium persulfate (APS, 99%) were supplied by J&K Scientific Co., Ltd. Pluronic F127 (99%) and cinnamaldehyde (95%) were obtained from Sinophar Chemical Reagent Co., Ltd. Nafion D-521 dispersion, Nafion N-117 membrane (0.180 mm thick, ≥ 0.90 meg/g exchange capacity), and Toray carbon paper (CP, TGP-H-60, 19 cm × 19 cm) were purchased from Alfa Aesar China Co., Ltd.

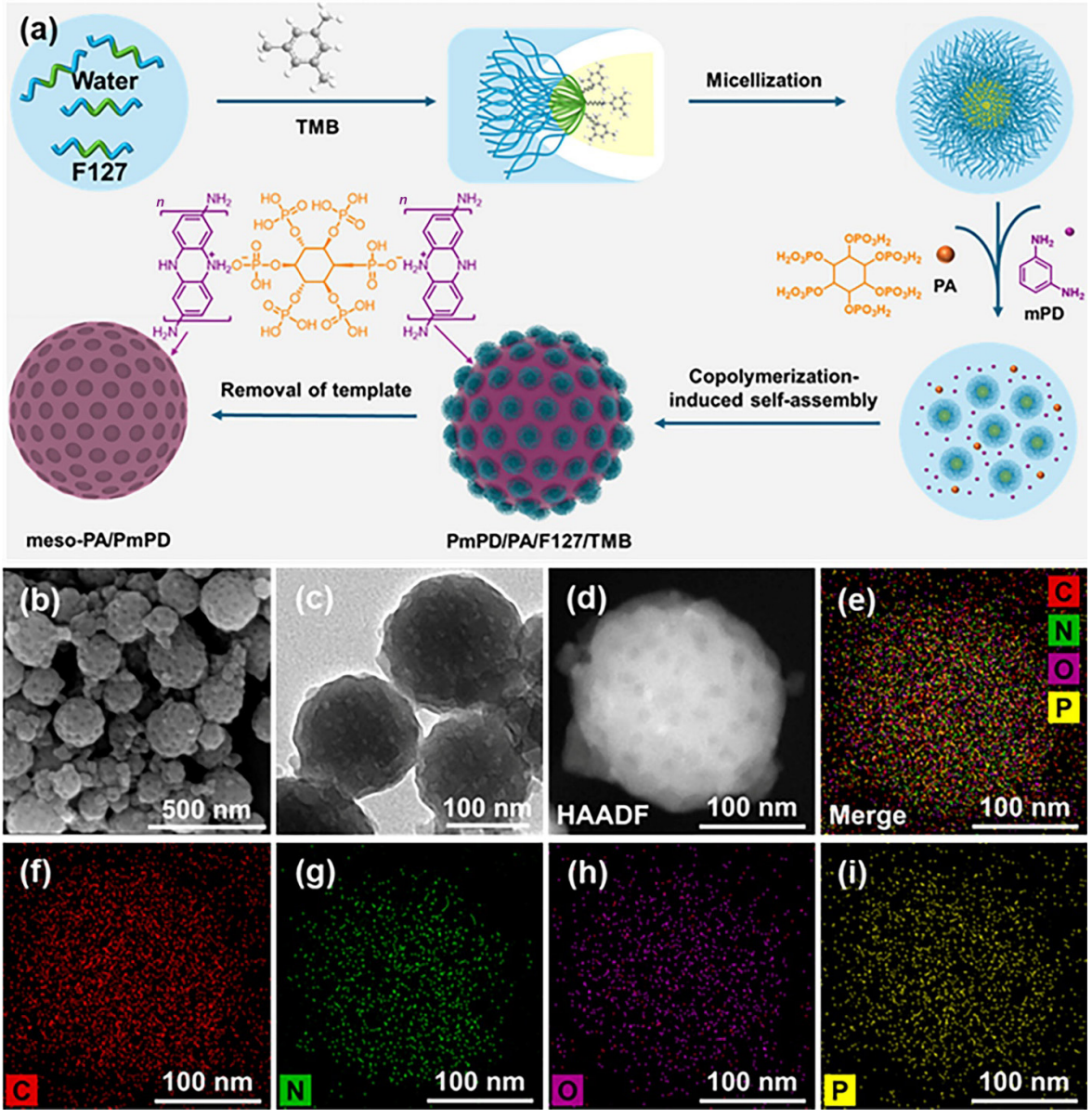

Figure 1 (a) Schematic diagram of the synthesis of meso-PA/PmPD composites. Structural characterizations of meso-PA(20)/PmPD nanospheres: (b) SEM image, (c) TEM image, and ((d)–(i)) element mapping images.

2.2 Preparation of meso-PA/PmPD nanospheres

Firstly, 300 mg of F127 was dissolved in deionized water (50 mL), and stirred with a magnetic stirrer at 500 rpm until the color was clear. Then, 300 mg of 1,3,5-trimethylbenzene (TMB) was added to the mixed solution. After 1 h, 100 mg of mPD was added. The mixture was stirred continuously for 1 h, then a certain amount of (0/5/10/15/20/25 μL) PA was added. After 1 h, 2 mL of APS (100 mg/mL) was added to the mixed solution to trigger the copolymerization self-assembly of m-phenylenediamine and PA. The mixture was stirred continuously for 24 h, and the resulting filtrate was centrifuged and washed with ethanol and water for 3 times to remove the F127 template and ammonium persulfate. The product was denoted as meso-PA/PmPD (e.g., meso-PA(0)/PmPD, meso-PA(5)/PmPD, meso-PA(10)/PmPD, meso-PA(15)/PmPD, meso-PA(20)/PmPD, and meso-PA(25)/PmPD, respectively).

3 Results and discussion

3.1 Preparation and characterizations of meso-PA/PmPD nanocomposites

The meso-PA/PmPD nanocomposites were prepared through a block copolymer templated self-assembly strategy [31, 32], which used Pluronic F127 copolymer as a soft template, TMB as a hydrophobic interaction mediation agent, mPD as monomers, and PA as a dopant (Fig. 1(a)). Typically, spherical micelles composed of F127/TMB were constructed by dissolving Pluronic F127 in water and then adding TMB [31]. After that, mPD and PA were introduced into the solution of the spherical micelles. Through the hydrogen bonding and electrostatic interaction, the precursors of the mPD and PA molecules can be adsorbed in the polyethylene oxide domain of Pluronic F127 to form mPD/PA/F127/TMB composites [31]. Under the initiation of APS, the

mPD/PA/F127/TMB composites were crosslinked and polymerized, forming a spherical polymeric structure. After removing the F127/TMB template, meso-PA/PmPD composites with a spherical mesoporous structure were obtained. By varying the doping amount of PA, a series of meso-PA/PmPD composites were prepared, including meso-PA(0)/PmPD, meso-PA(5)/PmPD, meso-PA(10)/PmPD, meso-PA(15)/PmPD, meso-PA(20)/PmPD, and meso-PA(25)/PmPD; the numbers in the sample names represent the amount of the added PA in the synthetic process of meso-PA/PmPD. The contents of PA in meso-PA/PmPD are determined by inductively coupled plasma spectroscopy and listed in Table S2 in the ESM. The detailed preparation procedures are described in the ESM.

The morphology of the meso-PA/PmPD nanocomposites was characterized by scanning electron microscopy (SEM) and transmission electron microscopy (TEM). As shown in Figs. 1(b) and 1(c), and Figs. S2–S7 in the ESM, the meso-PA/PmPD composites clearly display a spherical mesoporous structure. N_2 adsorption–desorption isotherm shows that the meso-PA/PmPD composites have different specific surface areas ranging from 95.3 to 48.6 m^2/g (Figs. S8–S13 and Table S3 in the ESM). In addition, Fourier transform infrared (FT-IR) was employed to further study the chemical nature of the meso-PA/PmPD composites (Figs. S14–S19 in the ESM). Taking meso-PA(20)/PmPD as an example (Fig. S14 in the ESM), it can be clearly observed that the wide peak at 3340 cm^{-1} belongs to the tensile vibrations of –NH– and –OH. The peaks at 1620, 1510, and 1220 cm^{-1} correspond to the tensile vibrations of the quinone, benzene, and C–N groups, respectively [33]. The peaks at 940 and 1065 cm^{-1} are caused by tensile vibrations of phosphate groups [34], indicating the doping of PA in meso-PA/PmPD. X-ray diffraction (XRD) pattern shows a weak and wide diffraction peak at ~ 24° corresponding to the (002) diffraction plane of carbon (Fig. S20 in the ESM), indicating an amorphous nature [35]. In addition, the element mapping images show the homogeneous distribution of C, N, O, and P elements in the meso-PA(20)/PmPD nanospheres (Figs. 1(d)–1(i)).

3.2 Electrocatalytic performance of meso-PA/PmPD for the CAL hydrogenation

Based on the structural advantages of meso-PA/PmPD composites and their potential electrocatalytic activity, the linear sweep voltammetry (LSV) measurement was initially used to evaluate the electrochemical activity of the meso-PA/PmPD composites toward the electrochemical hydrogenation of CAL. As shown in Fig. 2(a), when CAL was introduced into the cathode electrolyte system, the cathode current density increased significantly, indicating the occurrence of CAL hydrogenation. In addition, it can be observed that the cathode current density of meso-PA(20)/PmPD is higher than those of other meso-PA/PmPD samples (Fig. 2(a)), indicating that meso-PA(20)/PmPD delivers the highest response to the electrocatalytic hydrogenation of CAL. Gas chromatography-mass spectrometry (GC-MS) and ^1H nuclear magnetic resonance (NMR) analysis showed that HCOL was the main product accompanied with a very small amount of by-products, including phenylpropyl aldehyde (HCAL), COL, and the dimer (Figs. S21 and S22 in the ESM).

It is well known that the applied potential plays a crucial role in the performance of electrocatalytic reactions. Therefore, the effect of applied potential on the CAL hydrogenation over meso-PA(20)/PmPD was investigated. As shown in Fig. 2(b), the electrochemical hydrogenation of CAL to HCOL exhibits limited efficiency at a lower potential (−1.4 V), with low FE (66.4%) and selectivity (83.9%), accompanied by a low conversion (41.2%). With the increase of the applied potential, the conversion of CAL increases gradually, while the FE and selectivity of HCOL increase first and then decrease gradually. This phenomenon can be attributed to the fact that with an increase in the applied potential, more charges can be provided for the conversion of CAL, while high potentials (> −2.0 V) will accelerate the competitive hydrogen evolution reaction and the generation of by-products, thus leading to the decrease of FE and selectivity of HCOL. At −2.0 V vs. Ag/Ag^+, the FE and selectivity of HCOL reach the optimal values, which are 93.5% and 97.5%, respectively. In addition, the electrochemical performance of other meso-PA/PmPD composites (meso-PA(0)/PmPD, meso-PA(5)/PmPD, meso-PA(10)/PmPD, meso-PA(15)/PmPD, and meso-PA(25)/PmPD) for the CAL hydrogenation was also investigated. The corresponding results are given in Figs. S23–S27 in the ESM.

Figure 2(c) shows the effect of the different meso-PA/PmPD composites with different amounts of PA on the CAL hydrogenation. The meso-PA(20)/PmPD sample exhibits the best performance among all the meso-PA/PmPD samples. When using meso-PA(0)/PmPD without PA doping as an electrocatalyst, low FE (~ 73.5%) of HCOL was obtained. As the doping amount of PA increased within the range of 0–20, the FE and selectivity of HCOL gradually increased, while the conversion rate of CAL decreased first and then increased gradually. With the further increase of the PA amount (> 20), FE, selectivity, and conversion decreased. The reason can be that the excessive PA in meso-PA/PmPD can lead to a gradual increase in the size of meso-PA/PmPD nanospheres and a reduction in the pore size of nanospheres (Table S3 in the ESM), which significantly reduces the specific surface area of meso-PA/PmPD and ultimately decreases the exposure of active sites. Therefore, it can be concluded that an appropriate amount of PA in meso-PA/PmPD plays a key role in the catalytic performance. In addition, no obvious decrease in the FE, selectivity, and conversion of electrochemical hydrogenation of CAL to HCOL was observed after cycling for five times (Fig. 2(d)), indicating good cycling performance. TEM, FT-IR, and XPS characterizations reveal that the morphology and the chemical nature of meso-PA(20)/PmPD after use are basically identical to those of the fresh meso-PA(20)/PmPD (Figs. S28 and S29 in the ESM), indicating its excellent structural stability.

We also investigated the effect of charge quantity on the CAL hydrogenation by controlling the electrocatalytic time. As shown in Fig. 2(e), with the increase of charge quantity, the conversion of CAL gradually increases, and the selectivity of HCOL has no obvious change, while FE of HCOL significantly decreases. Particularly, when the charge consumption reaches 2Q (Q represents the stoichiometric amount of charge required to completely convert CAL to HCOL), the conversion of CAL reaches 89.1%, whereas FE of HCOL decreases to 40.7%. The possible reason is that the decreased concentration of CAL in the reaction system with the prolongation of electrolytic time could induce the enhancement of competitive hydrogen evolution reaction and result in a decrease in FE of HCOL. Furthermore, the catalytic performance of meso-PA(20)/PmPD at higher CAL concentrations was also evaluated. As shown in Fig. 2(f), FE and selectivity of HCOL decrease gradually with the increase of the CAL concentration. At the same time, it can be observed that the dimer

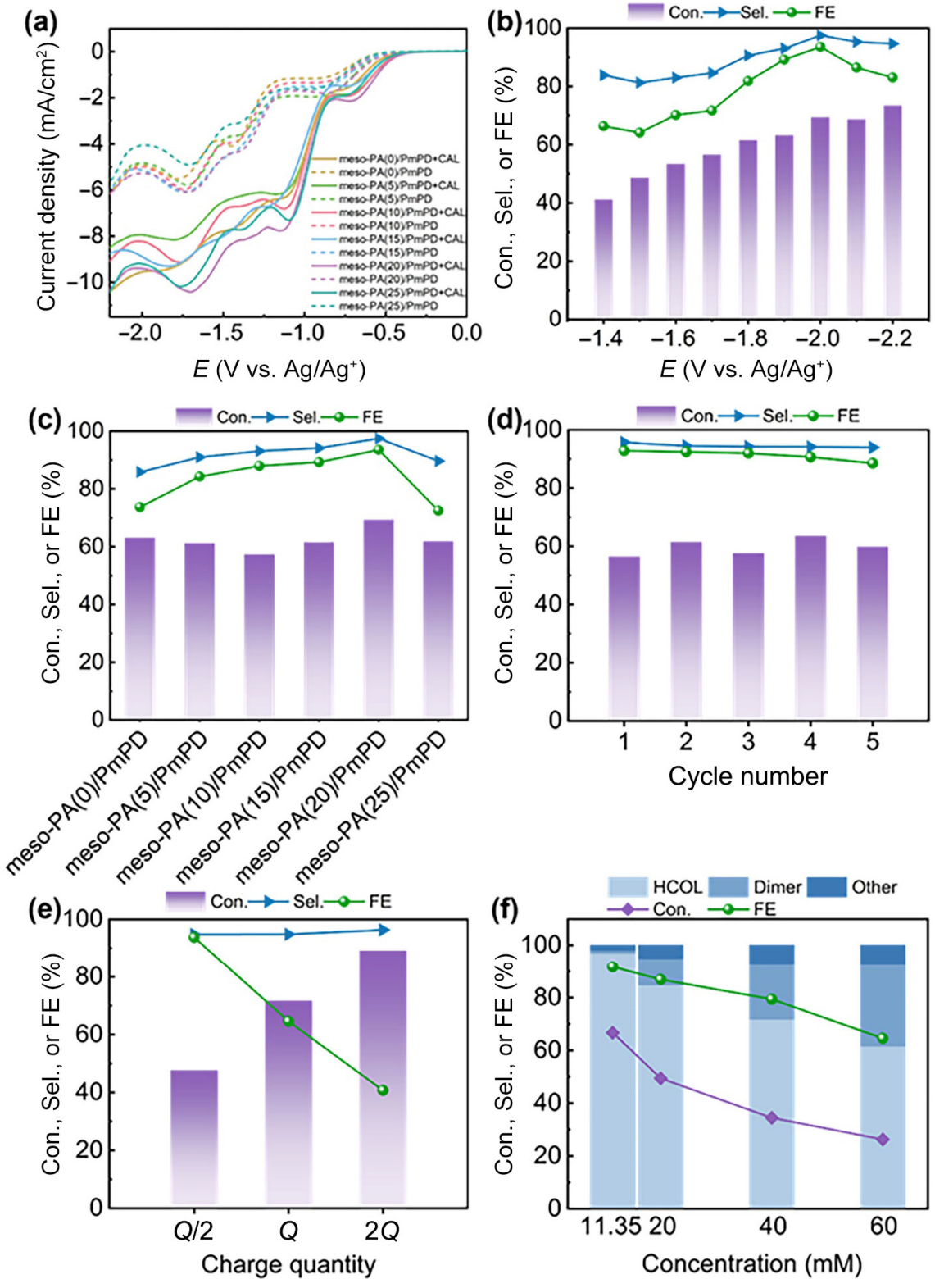

Figure 2 Performance evaluation of the meso-PA/PmPD composites for the CAL hydrogenation. (a) LSV measurements. (b) Effect of the applied potential over meso-PA(20)/PmPD. (c) Effect of the PA amount. (d) Cycling performance of meso-PA(20)/PmPD. (e) Effect of charge quantity. (f) Effect of the CAL concentration ("other" represents the trace by-products (phenylpropyl aldehyde and cinnamyl alcohol) generated during the electrocatalytic CAL reduction).

product from free CAL radical coupling gradually increases (Fig. S30 in the ESM) [36]. The reason could be that there is competitive adsorption of H* and CAL on the surface of meso-PA/PmPD. Due to the accumulation of a large amount of CAL on the cathode surface at high CAL concentrations, the coverage rate of H* would be reduced, which easily induces the formation of CAL dimer. This phenomenon is similar to that reported in literature, in which the degree of electric hydrodimerization enhances with the increase of

the CAL concentration [37, 38]. To mitigate the dimer formation during the high-concentration CAL electroreduction in future work, future studies could focus on two key strategies: (1) regulating catalyst active sites/surface properties and/or tailoring pore sizes of polymer-based catalysts to suppress intermediate coupling, and (2) employing flow reactors to enhance mass transfer and reduce local reactant concentration.

3.3 Mechanism investigation

Insights into the reaction mechanism are helpful for the understanding of electrochemical hydrogenation process of CAL. First, we employed Tafel plots to investigate the reaction kinetics. As shown in Fig. 3(a), the Tafel slope of meso-PA(20)/PmPD exhibits the smallest value (105.79 mV/dec) among those of the different meso-PA/PmPD samples (122.11 mV/dec for meso-PA(0)/PmPD, 161.26 mV/dec for meso-PA(5)/PmPD, 148.10 mV/dec for meso-PA(10)/PmPD, 121.18 mV/dec for meso-PA(15)/PmPD, and 132.07 mV/dec for meso-PA(25)/PmPD), indicating a fast reaction kinetic that is beneficial for accelerating the CAL reduction. In addition, the Tafel slopes of CAL electrochemical reduction over the meso-PA/PmPD samples are close to the benchmark value of 120 mV/dec, suggesting that the first proton-coupled electron transfer step acts as the rate-determining step [39, 40]. Meanwhile, the cyclic voltammetry (CV) measurements (Fig. S31 in the ESM) exhibit distinct desorption peaks of the adsorbed hydrogen (H*) species [41, 42], demonstrating that the hydrogen atoms generated via the proton-coupled electron transfer process are readily adsorbed onto the surface of meso-PA/PmPD, that is, proceeding through the Volmer step to form H* intermediates. Meanwhile, meso-PA(20)/PmPD exhibits the highest coverage of the H* species on the surface of meso-PA/PmPD due to its highest current density (Fig. S31 in the ESM). In addition, the electrochemical active surface areas of the meso-PA/PmPD composites were evaluated by double-layer capacitance method (C_{dl}). As shown in Fig. 3(b), the meso-PA(20)/PmPD has the highest C_{dl} value (0.22 mF/cm) among these meso-PA/PmPD composites (0.15 mF/cm^2 for meso-PA(0)/PmPD, 0.14 mF/cm^2 for meso-PA(5)/PmPD, 0.14 mF/cm^2 for meso-PA(10)/PmPD, 0.18 mF/cm^2 for meso-PA(15)/PmPD, and 0.17 mF/cm^2 for meso-PA(25)/PmPD), indicating that meso-PA(20)/PmPD has more catalytic active sites. Meanwhile, the N_2 adsorption–desorption analysis reveals that there is an obvious change in the specific surface areas of meso-PA/PmPD composites with the change of the PA amount (Table S3 in the ESM). These results indicate that the appropriate amount PA doping is conducive to the exposure of more active sites.

The advantage of the mesoporous structure of meso-PA/PmPD was also investigated. A control sample without mesoporous structure (denoted as non-PA(20)/PmPD) was synthesized as well, and the corresponding characterization results are shown in Fig. S32 in the ESM. LSV experiments of non-PA(20)/PmPD and meso-PA(20)/PmPD performed at different CAL concentrations revealed that the electrochemical reduction of CAL followed a diffusion-controlled process due to the increased cathode current density with the increase of the CAL concentration (Figs. S33 and S34 in the ESM) [43, 44]. Meanwhile, the current density of meso-PA(20)/PmPD is significantly higher than that of non-PA(20)/PmPD at different CAL concentrations (Figs. S33 and S34 in the ESM), indicating that the mesoporous structure contributes to enhancing the mass transfer of CAL, thus resulting in an increase in the current density of reaction. Moreover, the electrocatalytic performance of non-PA(20)/PmPD is generally inferior to that of meso-PA(20)/PmPD (Fig. S35 in the ESM). According to the LSV curves (Figs. S33 and S34 in the ESM) and relevant literature [36, 38], it is known that the nonporous structure of non-PA(20)/PmPD exhibits poor mass transfer of CAL, which may result in the increase of CAL concentration at the local reaction site caused by poor mass transfer. The elevated local concentration consequently induces a side reaction where CAL polymerizes to form a dimer, thus reducing the selectivity and FE of HCOL.

Electrochemical impedance spectroscopy (EIS) was also employed to study the charge transfer resistance of the meso-PA/PmPD composites in the CAL hydrogenation process. Figure 3(c) shows the Nyquist diagram of the meso-PA/PmPD composites at open circuit potential. It is seen that meso-PA(20)/PmPD shows the smallest semicircle among these meso-PA/PmPD composites, indicating a faster charge transfer at the interface of meso-PA(20)/PmPD and the cathode solution, which is beneficial for accelerating the reduction of CAL. *In-situ* EIS of meso-PA(20)/PmPD in the presence of CAL and N_2 was conducted to investigate the process of CAL reduction at −1.6 V vs. Ag/Ag$^+$ (Fig. 4(a)). After adding CAL to the electrolyte, the phase angle intensity of meso-PA(20)/PmPD is significantly lower than that without adding CAL. This phenomenon can be attributed to that the H* species generated *in-situ* by the water molecule dissociation react with the adsorbed CAL of high activity, which helps to inhibit the self-recombination of the H* species to H_2 [41].

The electrocatalytic processes of the CAL hydrogenation over meso-PA(20)/PmPD at different potentials were investigated by the *in-situ* Bode phase diagrams. As shown in Fig. S36 in the ESM, there is a distinct angular peak in the frequency region of 10–100 Hz, indicating that the interfacial charge transfer dominates

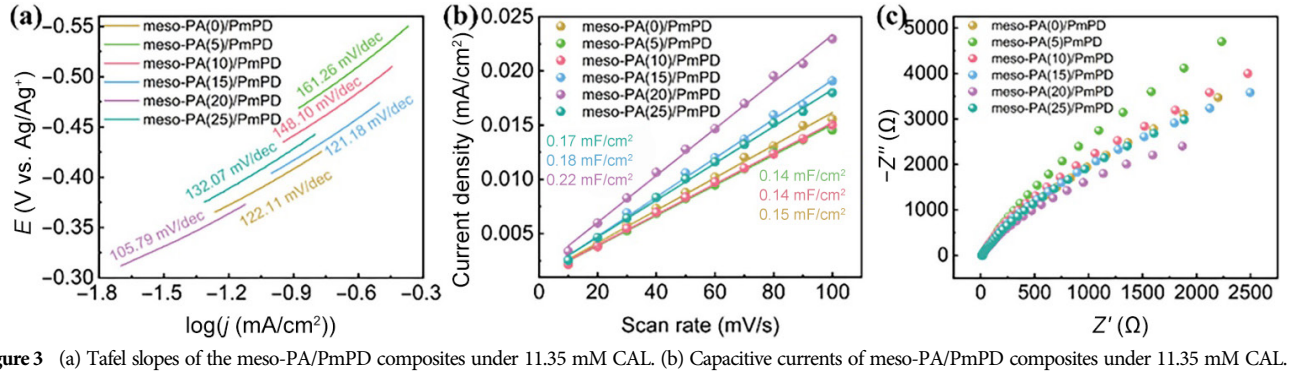

Figure 3 (a) Tafel slopes of the meso-PA/PmPD composites under 11.35 mM CAL. (b) Capacitive currents of meso-PA/PmPD composites under 11.35 mM CAL. (c) EIS spectra at open circuit potential.

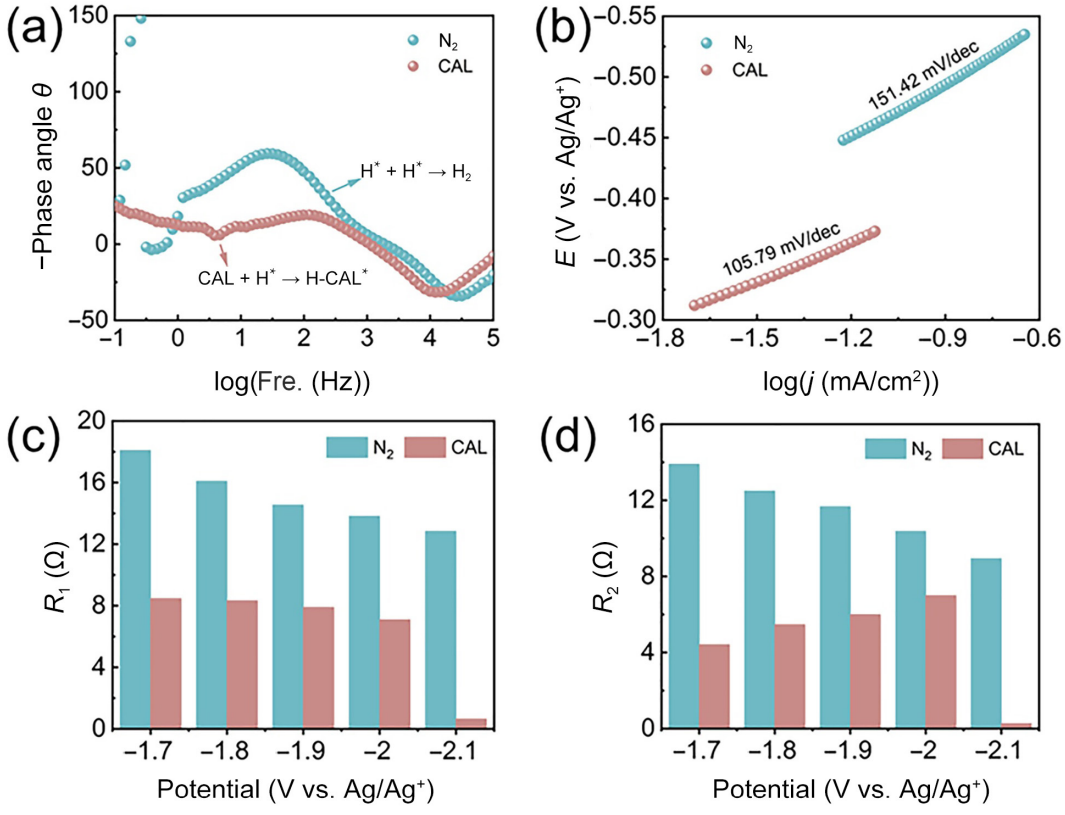

Figure 4 (a) *In-situ* Bode plots of meso-PA(20)/PmPD with or without CAL at −1.6 V vs. Ag/Ag$^+$. (b) Tafel plots of meso-PA(20)/PmPD with or without CAL. ((c) and (d)) The equivalent resistance of electrocatalytic hydrogenation of CAL over the meso-PA/PmPD composites at high potentials: (c) Volmer process and (d) interfacial reaction charge transfer process.

the entire reaction process [45–47]. In the range of −0.1–−0.5 V, the peak intensity of phase angle decreases with the increase of applied potential. This phenomenon is associated with the gradual generation of H* from the water dissociation [48]. As the applied potential further increases from −0.5 to −0.7 V, the peak intensity of the phase angle increases, possibly due to an increase in the number of H* occupied at the active site, thereby leading to a decrease in the number of accessible sites for producing H* [49, 50]. As the applied potential further increases (from −0.7 to −1.6 V), the peak intensity of the phase angle significantly decreases, which may be due to the accelerated dissociation of water at high potential to produce more H* species [41, 45], thus accelerating the reduction of CAL (Fig. 2(b)). In the range of −1.6–−1.9 V, the peak intensity increases and the peak slowly moves towards low frequencies, which is related to the uneven charge contribution produced by the reaction between the H* recombination and the interfacial reaction charge transfer of H* and CAL [37]. In the range of −1.9–−2.2 V, the peak intensity of phase angle decreases until the disappearance of phase angle peak, indicating the rapid depletion of H* species. Meanwhile, from the investigation of the potential (Fig. 2(b)), a large amount of CAL is converted in the range of −1.9–−2.2 V, indicating that the interfacial reaction charge transfer between CAL and H* is dominant in the electrocatalytic process compared to the H* self-recombination.

Figure 4(b) shows the Tafel plots of hydrogen evolution reaction and CAL electrochemical hydrogenation. It is seen that the Tafel slope of the CAL reduction (105.79 mV/dec) is lower than that of hydrogen evolution reaction (151.42 mV/dec), indicating that the electrochemical reduction of CAL is kinetically more favorable than hydrogen evolution reaction, which is conducive to inhibiting the recombination of H* species to generate H_2. Similar phenomenon was also observed in the reported literature [41, 51]. Based on these results, we proposed a simplified equivalent circuit to study the electrochemical hydrogenation behavior of meso-PA(20)/PmPD at high potentials (Figs. 4(c) and 4(d), and Fig. S37 in the ESM). The equivalent resistance of Volmer step (R_1) and the interfacial reaction charge transfer process (R_2) were investigated. As shown in Fig. 4(c), the value of R_1 in the presence of CAL is much smaller than that in the presence of N_2, indicating that H* species are rapidly consumed and the Volmer step of water molecule dissociation to H* is accelerated in the presence of CAL. In addition, in the presence of CAL, the value of R_2 is also significantly lower than that in N_2 environment (Fig. 4(d)), indicating that the interfacial reaction charge transfer between H* and CAL is more favorable than the self-recombination of the H* species. These results indicate that meso-PA(20)/PmPD prefers to enhance the reactivity of H* with CAL and inhibits the self-recombination of H* species.

Based on the experimental results, we propose two reaction pathways for the electrocatalytic hydrogenation of CAL to HCOL over meso-PA/PmPD composites. As shown in Fig. 5(a), pathway a involves the preferential hydrogenation of CAL C=C bond to HCAL as the intermediate. Then the HCAL aldehyde group is hydrogenated to HCOL. Pathway b (Fig. 5(b)) involves the formation of COL as the intermediate by the preferential hydrogenation of CAL aldehyde group and H*. Subsequently, the C=C bond of COL is subjected to further hydrogenation to form HCOL. In both of the pathways, the step of water dissociation to generate H* species is promoted, accompanied by the electron

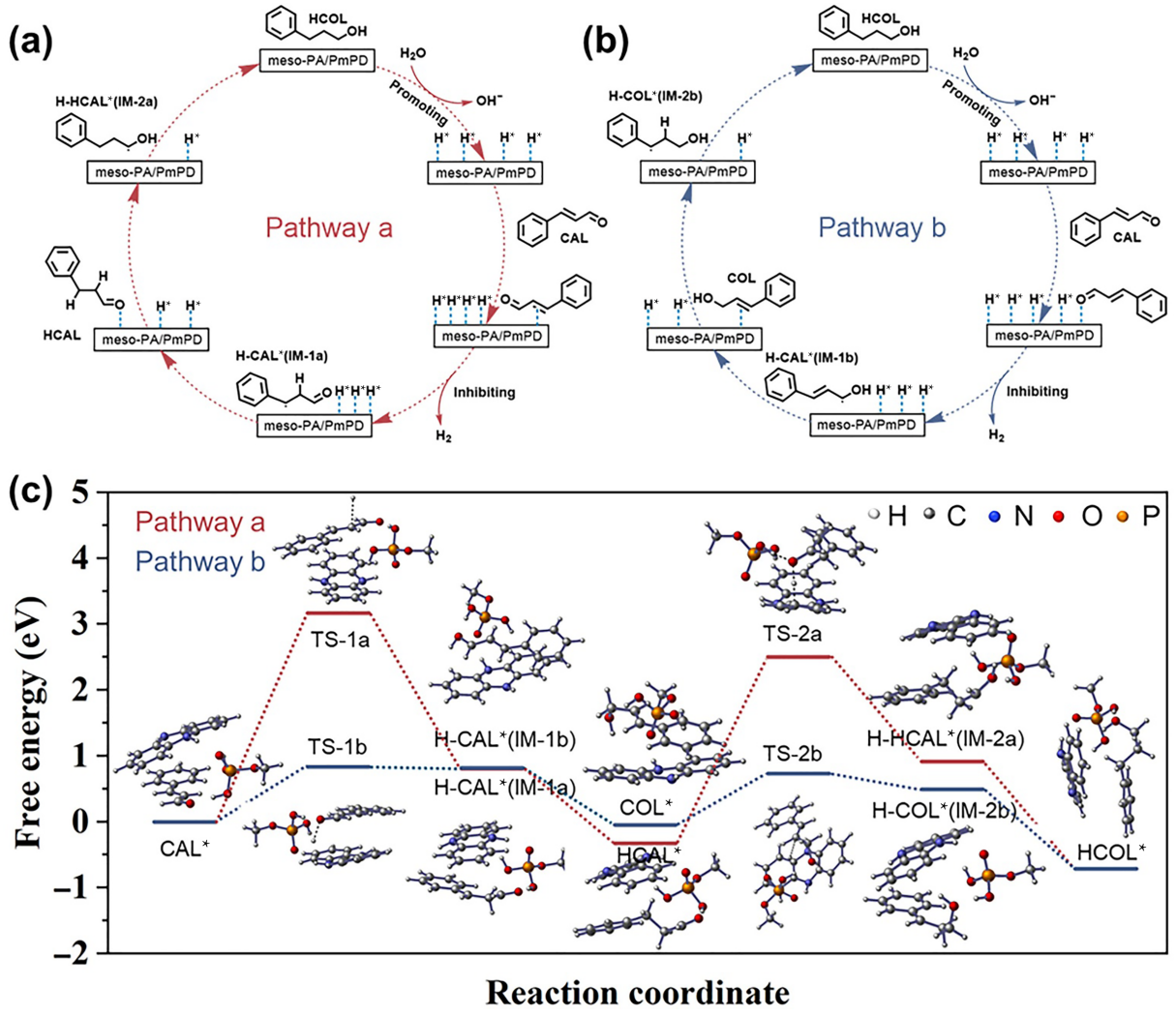

Figure 5 ((a) and (b)) Mechanisms of the CAL hydrogenation on meso-PA/PmPD. (c) Gibbs free energy diagram of the CAL hydrogenation on the meso-PA/PmPD surface.

transfer process on the surface of meso-PA/PmPD, thus enhancing the coverage of H* on the meso-PA/PmPD surface. For pathway a, the H* species react with the C=C bond of CAL adsorbed on the meso-PA/PmPD surface to form H-CAL*(IM-1a) through the electrocatalytic hydrogenation mechanism. Due to the faster reaction kinetics of H* species and CAL, the recombination step of H* can be efficiently inhibited. The H-CAL*(IM-1a) is further hydrogenated with the second H* to form HCAL. Then the C=O group of HCAL couples with a H* to form H-HCAL*(IM-2a), and then is converted to HCOL. For pathway b, the C=O group of CAL prefers to adsorb on the surface of meso-PA/PmPD and reacts with H* to form H-CAL*(IM-1b). The resulting H-CAL*(IM-1b) is further hydrogenated with the second H* to form COL. Then the C=C group of COL is coupled with a H* to form H-COL*(IM-2b), which is subsequently further converted to HCOL.

Density functional theory (DFT) calculations were used to gain deeper insight into the CAL reduction process. The simplified surface fragments of the catalyst with/without the PA doping were employed due to their periodicities. Figure 5(c) and Fig. S38 in the ESM show the free energy of the reduction of CAL to HCOL via the two pathways (pathways a and b). For pathway a (Fig. 5(c)), meso-PA/PmPD requires high energy barriers for the protonation of the CAL* C=C bond (TS-1a, 3.17 eV), which is much higher than that of pathway b, namely, the protonation of the CAL* aldehyde group (TS-1b, 0.83 eV). In addition, in pathway a, the Gibbs free energy change for the intermediate HCAL* protonation process was 2.83 eV (TS-2a), while the intermediate COL* protonation process exhibited a Gibbs free energy change of 0.77 eV (TS-2b). Therefore, it is considered that meso-PA/PmPD catalyzes the electrochemical hydrogenation of CAL mainly through pathway b. For comparison, the meso-PA(0)/PmPD without doping PA was also studied. In pathway a (Fig. S38 in the ESM), the Gibbs free energy change for the CAL* C=C bond process was 2.55 eV (TS-1a′). However, for pathway b (Fig. S38 in the ESM), the Gibbs free energy change for the formation of TS-1b′ process was 3.07 eV. The results indicated that incorporating PA into meso-PA/PmPD can reduce the energy barriers for the hydrogenation of CAL* aldehyde group with H* to the H-CAL* (IM-1b) and subsequent hydrogenation of the COL* intermediate to the intermediate H-COL* (IM-2b). In addition, Fig. S39 in the ESM shows that whether or not incorporating PA into the meso-PA/PmPD, it can induce the parallel-configuration adsorption of CAL on their surface through the π–π interaction. According to literature, the parallel-configuration adsorption of CAL is

conducive to the formation of HCOL. Adsorption energy calculations (Fig. S39 in the ESM) demonstrate that the PA doping can enhance the adsorption of CAL. The optimized configuration indicates that the enhanced adsorption of CAL can be attributed to the hydrogen-bonding interaction between the CAL aldehyde group and PA (Fig. S40 in the ESM), which is helpful for the activation of the CAL aldehyde group and induces its preferential hydrogenation, namely, pathway b. These results explain the higher activity of meso-PA/PmPD for the HCOL production in our experiment. Based on the above analysis, the π–π stacking interactions between the aromatic moieties of the catalyst and the conjugated structure of CAL play a pivotal role in substrate adsorption and activation. Therefore, π-conjugated polymers-based catalysts with extended aromatic frameworks (e.g., covalent organic frameworks with triazine or benzene building blocks and conjugated microporous polymers) are promising candidates for this reaction.

4 Conclusions

In summary, a series of PA-doped metal-free mesoporous polymer-based meso-PA/PmPD composites were constructed through a block copolymer templated self-assembly strategy. The optimized meso-PA/PmPD exhibited an excellent electrocatalytic performance for the electrochemical reduction of CAL to HCOL, with high FE (93.5%) and selectivity (97.5%). Mechanistic studies revealed that the parallel-configuration adsorption of CAL caused by the π–π and hydrogen-bonding interactions reduced the energy barriers for the hydrogenation of CAL carbonyl group toward COL intermediate and subsequent hydrogenation of COL to HCOL. Moreover, an appropriate amount of PA could accelerate the water dissociation to generate H* species and interfacial charge transfer rate. Meanwhile, the mesoporous polymeric structure of meso-PA/PmPD improved the mass transport of CAL into catalyst. These synergistic effects collectively delivered the excellent performance. This work opens a new avenue for developing polymer-based electrocatalysts to efficiently convert biomass into high-value-added chemicals and provides insightful clues to help understanding complex biomass conversion mechanisms.

Electronic Supplementary Material: Supplementary material (materials, experimental methods, DFT calculations, and supporting tables and figures) is available in the online version of this article at https://doi.org/10.26599/NR.2026.94908452.

Data availability

All data needed to support the conclusions in the paper are presented in the manuscript and the Electronic Supplementary Material. Additional data related to this paper may be requested from the corresponding author upon request.

Acknowledgements

This work was supported by the National Natural Science Foundation of China (Nos. 22408346, 22225501, W2412102, and 52421006), the Science and Technology Research Project of Henan Province (Nos. 242102320375 and 252102321168), the Shanghai Municipal Science and Technology Major Project, and SJTU 2030B plan (No. WH510207202).

Declaration of competing interest

All the contributing authors report no conflict of interests in this work.

Author contribution statement

H. R. W. and R. L. Y. designed the project. R. L. Y. was responsible for data collection and analysis. C. S., T. Y. X., and C. L. assisted with data analysis. H. S. X. provided support for the acquisition of TEM and SEM images. Supervision of the research was provided by W. X. Z. and Y. Y. M. All the authors have approved the final manuscript.

Use of AI statement

None.

References

[1] Chauhan, A.; Srivastava, R. Biomass valorization with metal-free catalysts: Innovations in thermocatalytic, photocatalytic, and electrocatalytic approaches. *Chem. Soc. Rev.* **2025**, *54*, 7114–7173.

[2] Barbará, P. V.; Choudhary, H.; Nakasu, P. S.; Al-Ghatta, A.; Han, Y. L.; Hopson, C.; Aravena, R. I.; Mishra, D. K.; Ovejero-Pérez, A.; Simmons, B. A. et al. Recent advances in the use of ionic liquids and deep eutectic solvents for lignocellulosic biorefineries and biobased chemical and material production. *Chem. Rev.* **2025**, *125*, 5461–5583.

[3] Zheng, S. S.; Zhang, Z. L.; He, S. B.; Yang, H. Z.; Atia, H.; Abdel-Mageed, A. M.; Wohlrab, S.; Baráth, E.; Tin, S.; Heeres, H. J. et al. Benzenoid aromatics from renewable resources. *Chem. Rev.* **2024**, *124*, 10701–10876.

[4] Zhou, H. Y.; Kunzendorf, A.; Xu, G. C.; Frietema, H. O. T.; Thunnissen, A. M. W. H.; Poelarends, G. J. Engineering 2-deoxy-D-ribose-5-phosphate aldolase for anti- and syn-selective epoxidations of α,β-unsaturated aldehydes. *Angew. Chem., Int. Ed.* **2025**, *64*, e202503054.

[5] Wang, Y. P.; Huang, Y. Q.; Song, L. P.; Wang, H.; Wan, L.; Pang, J. Q.; Liang, W. J. The characteristic VOCs of different parts of *Artocarpus heterophyllus* fruit based on HS-SPME-GC-MS and PTR-TOF-MS. *Food Chem.* **2024**, *459*, 140431.

[6] Dong, Z.; Nakagawa, Y.; Liu, B.; Mihara, S.; Yabushita, M.; Tomishige, K. Selective C=O hydrogenation of cinnamaldehyde over Ir-based catalysts and its comparison with C–O hydrogenolysis of polyols. *Catal. Sci. Technol.* **2025**, *15*, 2527–2543.

[7] Wang, L. W.; Ma, Y. F.; Li, H. T.; Luo, W. H.; Liu, J. Screening support effect of Pt/MO_x for selective hydrogenation of cinnamaldehyde. *J. Catal.* **2024**, *431*, 115391.

[8] Choi, M.; Bae, S.; Kim, Y.; Lee, Y.; Cho, M.; Kang, S.; Lee, J. Selective formaldehyde condensation on phosphorus-rich copper catalyst to produce liquid C_{3+} chemicals in electrocatalytic CO_2 reduction. *Nat. Catal.* **2025**, *8*, 476–486.

[9] Wan, C. Z.; Ager, J. W.; Huang, Y. Hydrogen transfer pathway controls selectivity in electrocatalytic CO_2 reduction. *Nat. Chem.* **2025**, *17*, 307–308.

[10] Tian, C.; Yu, J. Q.; Zhou, D. J.; Ze, H. J.; Liu, H. Z.; Chen, Y. J.; Xia, R.; Ou, P. F.; Ni, W. Y.; Xie, K. et al. Reduction of 5-hydroxymethylfurfural to 2,5-bis(hydroxymethyl)furan at high current density using a Ga-doped AgCu: Cationomer hybrid electrocatalyst. *Adv. Mater.* **2024**, *36*, 2312778.

[11] Majhi, K. C.; Chen, H. J.; Batool, A.; Zhu, Q.; Jin, Y. X.; Liu, S. Q.; Sit, P. H. L.; Lam, J. C. H. In-tandem electrochemical reduction of nitrate to ammonia on ultrathin-sheet-assembled iron-nickel alloy nanoflowers. *Angew. Chem., Int. Ed.* **2025**, *64*, e202500167.

[12] Lin, J.; Liu, Z. P.; Wu, H. F.; Wang, Z. Q.; Wang, G. Q.; Bu, J.;

Wang, Y. N.; Liu, P.; Wang, J. J.; Zhang, J. Efficient electroreduction of carbonyl compounds to alcohols over Fe/Fe_2O_3 interfaces. *Nat. Catal.* **2025**, *8*, 338–347.

[13] Chen, L.; Yu, C.; Dong, J. T.; Han, Y. N.; Huang, H. L.; Li, W. B.; Zhang, Y. F.; Tan, X. Y.; Qiu, J. S. Seawater electrolysis for fuels and chemicals production: Fundamentals, achievements, and perspectives. *Chem. Soc. Rev.* **2024**, *53*, 7455–7488.

[14] Wang, J. L.; Jin, M.; Sun, Y. Y.; Zhang, H. M. Pt-Modified MoO_3 catalyst for the electrochemically selective C=O hydrogenation of cinnamaldehyde. *Chem. Commun.* **2022**, *58*, 6721–6724.

[15] Zhang, Q. Q.; Sun, Y. F.; Li, W.; Zhang, J. L.; Fu, Y. Highly selective electrocatalytic hydrogenation of cinnamaldehyde over tin dioxide-supported palladium nanocatalysts. *Int. J. Hydrogen Energy* **2022**, *47*, 38229–38241.

[16] Wu, T. X.; Meng, H. Q.; Dang, R. Amorphous Ta_2O_5-supported Ru as an efficient electrocatalyst for selective hydrogenation of cinnamaldehyde with water as the hydrogen source. *Inorg. Chem. Front.* **2021**, *8*, 4712–4719.

[17] Wu, T. X.; Han, M. M. Vapor-phase hydrothermal construction of defective MoS_2 for highly selective electrocatalytic hydrogenation of cinnamaldehyde. *Mater. Adv.* **2022**, *3*, 8250–8259.

[18] Yuan, X. S.; Zhou, S. H.; Wang, S. M.; Wei, W. B.; Li, X. F.; Wu, X. T.; Zhu, Q. L. Ordered macroporous superstructure of defective carbon adorned with tiny cobalt sulfide for selective electrocatalytic hydrogenation of cinnamaldehyde. *Appl. Catal. B: Environ. Energy* **2025**, *361*, 124642.

[19] Lu, C. B.; He, Q. C.; Huang, S. H.; Shi, P. F.; Yang, C. Q.; Zhang, J. C.; Zhu, J. H.; Zhang, J.; Wang, T. F.; Zhuang, X. D. Large dipole moment enhanced CO_2 adsorption on copper surface: Achieving 68.9% catalytic ethylene faradaic efficiency at 1.0 $A \cdot cm^{-2}$. *Adv. Mater.* **2025**, *37*, 2415092.

[20] Liu, X.; Li, B.; Han, G. Q.; Liu, X. W.; Cao, Z.; Jiang, D. E.; Sun, Y. J. Electrocatalytic synthesis of heterocycles from biomass-derived furfuryl alcohols. *Nat. Commun.* **2021**, *12*, 1868.

[21] Wu, H. R.; Zou, Y. S.; Xu, H. S.; Wu, L.; Mai, Y. Y. Efficient Electrocatalytic Upgradation of furan-based biomass: Key roles of a two-dimensional mesoporous poly(m-phenylenediamine)-graphene heterostructure and a ternary electrolyte. *Macromolecules* **2022**, *55*, 1445–1456.

[22] Yamaguchi, S.; Kamiya, K.; Hashimoto, K.; Nakanishi, S. Ru atom-modified covalent triazine framework as a robust electrocatalyst for selective alcohol oxidation in aqueous electrolytes. *Chem. Commun.* **2017**, *53*, 10437–10440.

[23] Yang, D. H.; Tao, Y.; Ding, X. S.; Han, B. H. Porous organic polymers for electrocatalysis. *Chem. Soc. Rev.* **2022**, *51*, 761–791.

[24] Zhao, Q.; Zhang, Q. X.; Xu, Y. H.; Han, A. H.; He, H. W.; Zheng, H. Q.; Zhang, W.; Lei, H. T.; Apfel, U. P.; Cao, R. Improving active site local proton transfer in porous organic polymers for boosted oxygen electrocatalysis. *Angew. Chem., Int. Ed.* **2024**, *63*, e202414104.

[25] Chen, T. F.; Zhang, W. X.; Li, B.; Huang, W. B.; Lin, C. H.; Wu, Y.; Chen, S. H.; Ma, H. P. Adsorptive separation of aromatic compounds from alkanes by π–π interactions in a carbazole-based conjugated microporous polymer. *ACS Appl. Mater. Interfaces* **2020**, *12*, 56385–56392.

[26] Che, H. N.; Wang, J.; Wang, P. F.; Ao, Y. H.; Chen, J.; Gao, X.; Zhu, F. Y.; Liu, B. Simultaneously achieving fast intramolecular charge transfer and mass transport in holey D-π-A organic conjugated polymers for highly efficient photocatalytic pollutant degradation. *JACS Au* **2023**, *3*, 1424–1434.

[27] Zeng, Y. X.; Pei, Z. H.; Guo, Y.; Luan, D. Y.; Gu, X. J.; Lou, X. W. Zincophilic interfacial manipulation against dendrite growth and side reactions for stable Zn metal anodes. *Angew. Chem., Int. Ed.* **2023**, *62*, e202312145.

[28] Ballabio, M.; Zhang, T.; Chen, C.; Zhang, P.; Liao, Z. Q.; Hambsch, M.; Mannsfeld, S. C. B.; Zschech, E.; Sirringhaus, H.; Feng, X. L. et al. Band-like charge transport in phytic acid-doped polyaniline thin films. *Adv. Funct. Mater.* **2021**, *31*, 2105184.

[29] Hu, Q.; Li, G. M.; Liu, X. F.; Zhu, B.; Chai, X. Y.; Zhang, Q. L.; Liu, J. H.; He, C. X. Superhydrophilic phytic-acid-doped conductive hydrogels as metal-free and binder-free electrocatalysts for efficient water oxidation. *Angew. Chem., Int. Ed.* **2019**, *58*, 4318–4322.

[30] Lohani, P. C.; Tiwari, A. P.; Muthurasu, A.; Pathak, I.; Poudel, M. B.; Chhetri, K.; Dahal, B.; Acharya, D.; Ko, T. H.; Kim, H. Y. Phytic acid empowered two nanos "polypyrrole tunnels and transition metal-(oxy)hydroxide sheets" in a single platform for unmitigated redox water splitting. *Chem. Eng. J.* **2023**, *463*, 142280.

[31] Liu, Y. M.; Zhang, L. L.; Tan, Z. W.; Sun, W. Y.; Zhang, L.; Qiao, Z. A. Molecular-level modulation of N, S-co-doped mesoporous carbon nanospheres for selective aqueous catalytic oxidation of ethylbenzene. *Angew. Chem., Int. Ed.* **2025**, *64*, e202419438.

[32] Xiang, L. X.; Li, Q.; Li, C.; Yang, Q. Q.; Xu, F. G.; Mai, Y. Y. Block copolymer self-assembly directed synthesis of porous materials with ordered bicontinuous structures and their potential applications. *Adv. Mater.* **2023**, *35*, 2207684.

[33] Zha, X. L.; Xu, G. L.; Xiong, Y.; Yan, Z.; Liu, K.; Li, M. F.; Chen, Y. L.; Lu, J.; Wang, D. Modulating the macroscopic helicity of poly(m-phenylenediamine) by achiral monomer copolymerization. *Adv. Funct. Mater.* **2023**, *33*, 2211956.

[34] Feng, K. R.; Meng, L. X.; Xu, J. M.; Zhao, P. Y.; Li, N.; Lei, J. X. Introduction of bifunctionalized UIO-66-NH_2 for highly conductive and long-term stable fluorene-based sulfonated poly(aryl ether ketone sulfone) PEMs. *ACS Appl. Polym. Mater.* **2024**, *6*, 10916–10926.

[35] Tian, J. Q.; Luo, Y. L.; Li, H. L.; Lu, W. B.; Chang, G. H.; Qin, X. Y.; Sun, X. P. Ag@poly(m-phenylenediamine)-Ag core–shell nanoparticles: One-step preparation, characterization, and their application for H_2O_2 detection. *Catal. Sci. Technol.* **2011**, *1*, 1393–1398.

[36] Huang, X.; Zhang, L.; Li, C. P.; Tan, L. Q.; Wei, Z. D. High selective electrochemical hydrogenation of cinnamaldehyde to cinnamyl alcohol on RuO_2-SnO_2-TiO_2/Ti electrode. *ACS Catal.* **2019**, *9*, 11307–11316.

[37] Chen, J. H.; Wu, S. L.; Pan, X.; Zhou, X.; Zhang, X. C. Electrochemical reduction hydrogenation, hydrogenolysis and dimerization of bio-derived aldehydes: A review. *Renew. Sustain. Energy Rev.* **2025**, *207*, 114900.

[38] Huang, S. Q.; Gong, B.; Jin, Y. X.; Sit, P. H. L.; Lam, J. C. H. The structural phase effect of MoS_2 in controlling the reaction selectivity between electrocatalytic hydrogenation and dimerization of furfural. *ACS Catal.* **2022**, *12*, 11340–11354.

[39] Lin, X.; Hu, F. S.; Li, Q. Y.; Xu, D.; Xu, Y. S.; Zhang, Z.; Chen, J. S.; Li, X. H. Electron divergence of $Cu^{\delta-}$ and $Pd^{\delta+}$ in Cu_3Pd alloy-based heterojunctions boosts concerted C≡C bond binding and the volmer step for alkynol semihydrogenation. *J. Am. Chem. Soc.* **2024**, *146*, 18451–18458.

[40] Lao, M. M.; Rui, K.; Zhao, G. Q.; Cui, P. X.; Zheng, X. S.; Dou, S. X.; Sun, W. P. Platinum/nickel bicarbonate heterostructures towards accelerated hydrogen evolution under alkaline conditions. *Angew. Chem., Int. Ed.* **2019**, *58*, 5432–5437.

[41] Ji, K. Y.; Xu, M.; Xu, S. M.; Wang, Y.; Ge, R. X.; Hu, X. Y.; Sun, X. M.; Duan, H. H. Electrocatalytic hydrogenation of 5-hydroxymethylfurfural promoted by a Ru_1Cu single-atom alloy catalyst. *Angew. Chem., Int. Ed.* **2022**, *61*, e202209849.

[42] Xu, S. L.; Wang, W.; Li, H. T.; Gao, Y. X.; Min, Y.; Liu, P. G.; Zheng, X. S.; Liu, D. F.; Chen, J. J.; Yu, H. Q. et al. Electrocatalytic hydrogenation boosted by surface hydroxyls-modulated hydrogen migration over nonreducible oxides. *Adv. Mater.* **2025**, *37*, 2500371.

[43] Pang, X. L.; Bai, H. Y.; Zhao, H. Q.; Fan, W. Q.; Shi, W. D. Efficient electrocatalytic oxidation of 5-hydroxymethylfurfural coupled with 4-nitrophenol hydrogenation in a water system. *ACS Catal.* **2022**, *12*, 1545–1557.

[44] Dai, H. L.; Huang, Y. F.; Bai, H. Y.; Li, H. P.; Zhao, H. Q.; Wang, F. G.; Fan, W. Q.; Shi, W. D. Adsorption–activation bifunctional center of Al/Co-base catalyst for boosting 5-hydroxymethylfurfural oxidation. *Adv. Energy Mater.* **2024**, *14*, 2402789.

[45] Xie, C.; Chen, W.; Du, S. Q.; Yan, D. F.; Zhang, Y. Q.; Chen, J.; Liu, B.; Wang, S. Y. *In-situ* phase transition of WO_3 boosting electron and hydrogen transfer for enhancing hydrogen evolution on Pt. *Nano Energy* **2020**, *71*, 104653

[46] Huang, L. L.; Chen, D. W.; Luo, G.; Lu, Y. R.; Chen, C.; Zou, Y. Q.; Dong, C. L.; Li, Y. F.; Wang, S. Y. Zirconium-regulation-induced bifunctionality in 3D cobalt-iron oxide nanosheets for overall water splitting. *Adv. Mater.* **2019**, *31*, 1901439.

[47] Zhang, Q.; Zhang, X. J.; Liu, B. C.; Jing, P.; Xu, X.; Hao, H. G.; Gao, R.; Zhang, J. Active hydroxyl-mediated preferential cleavage of carbon–carbon bonds in electrocatalytic glycerol oxidation. *Angew. Chem., Int. Ed.* **2025**, *64*, e202420942.

[48] Dasgupta, B.; Bagchi, D.; Sontheimer, T.; Driess, M.; Menezes, P. W. Dynamics in electrochemical organic oxidation reactions from *in situ* and operando techniques. *Nat. Rev. Chem.* **2025**, *9*, 766–789.

[49] Chen, W.; Xie, C.; Wang, Y. Y.; Zou, Y. Q.; Dong, C. L.; Huang, Y. C.; Xiao, Z. H.; Wei, Z. X.; Du, S. Q.; Chen, C. et al. Activity origins and design principles of nickel-based catalysts for nucleophile electrooxidation. *Chem* **2020**, *6*, 2974–2993.

[50] Sanyal, U.; Yuk, S. F.; Koh, K.; Lee, M. S.; Stoerzinger, K.; Zhang, D. F.; Meyer, L. C.; Lopez-Ruiz, J. A.; Karkamkar, A.; Holladay, J. D. et al. Hydrogen bonding enhances the electrochemical hydrogenation of benzaldehyde in the aqueous phase. *Angew. Chem., Int. Ed.* **2021**, *60*, 290–296.

[51] Lv, S. J.; Lu, Y. J.; Guo, X. B.; Wang, K.; Jiang, J. C.; Xu, J. M. Ru/TiO_2 Combined with self-reconstructing copper nanowires for efficient and stable electroreduction of 5-hydroxymethylfurfural. *ACS Sustain. Chem. Eng.* **2025**, *13*, 10611–10621.